Available online at www.sciencedirect.com
ScienceDirect
Magnetic Resonance Imaging 28 (2010) 77 – 86
MAGNETIC RESONANCE IMAGING

High-definition, single-scan 2D MRI in inhomogeneous fields using spatial encoding methods

Noam Ben-Eliezer, Yoav Shrot, Lucio Frydman*

Chemical Physics Department, Weizmann Institute of Science, Rehovot 76100, Israel

Received 25 December 2008; revised 8 March 2009; accepted 10 May 2009

Abstract

An approach has been recently introduced for acquiring two-dimensional (2D) nuclear magnetic resonance images in a single scan, based on the spatial encoding of the spin interactions. This article explores the potential of integrating this spatial encoding together with conventional temporal encoding principles, to produce 2D single-shot images with moderate field of views. The resulting "hybrid" imaging scheme is shown to be superior to traditional schemes in non-homogeneous magnetic field environments. An enhancement of previously discussed pulse sequences is also proposed, whereby distortions affecting the image along the spatially encoded axis are eliminated. This new variant is also characterized by a refocusing of T_2* effects, leading to a restoration of high-definition images for regions which would otherwise be highly dephased and thus not visible. These single-scan 2D images are characterized by improved signal-to-noise ratios and a genuine T_2 contrast, albeit not free from inhomogeneity distortions. Simple postprocessing algorithms relying on inhomogeneity phase maps of the imaged object can successfully remove most of these residual distortions. Initial results suggest that this acquisition scheme has the potential to overcome strong field inhomogeneities acting over extended acquisition durations, exceeding 100 ms for a single-shot image.

Keywords: MRI methodologies; Ultrafast imaging; Spatial encoding; Field inhomogeneities

1. Introduction

The expanding scope of nuclear magnetic resonance imaging (MRI) poses increasing challenges and demands from modern scanners. One of the most prominent examples of such demands is furnished by echo planar imaging (EPI), a widely used technique capable of delivering two-dimensional (2D) nuclear magnetic resonance (NMR) images in a single scan [1–3]. EPI's ability to acquire full images in short timescales has had a sizeable impact on functional MRI's clinical and research applications [4,5]. Notwithstanding, this increased use, EPI still faces a number of challenges, particularly when dealing with multiple sites at high fields, or when operating in non-homogeneous magnetic fields. Such settings are characterized by short T_2* values associated to chemical-shift distributions or susceptibility artifacts, causing a rapid transverse spin dephasing that may act as major source of image distortions. Numerous approaches have been proposed for dealing with such artifacts including echoing sequences, spiral sampling strategies, segmented *k*-space sampling, and post-processing deconvolution algorithms [6–9]. These are all capable of alleviating image distortions to some extent, but are still challenged by high inhomogeneity regions producing low-intensity or highly distorted signals.

Among the alternatives proposed for performing ultrafast, single-shot imaging [10,11] counts a scheme based on imparting a spatial rather than a temporal encoding of the spin interactions [12]. Initially developed as a general approach for acquiring arbitrary 2D NMR spectra within a single scan [13,14], this method can also be exploited within the context of pure MRI. One of the main potential advantages of this spatial-encoded imaging method relates to its locality. This property is manifested by an ability to specifically address different locations within the sample at different times, both during the excitation and during acquisition events. This feature has been shown to have two potential — and somewhat related — applications

* Corresponding author. Tel.: +972 8 9344903; fax: +972 8 9344123.
E-mail address: lucio.frydman@weizmann.ac.il (L. Frydman).

0730-725X/$ – see front matter © 2010 Elsevier Inc. All rights reserved.
doi:10.1016/j.mri.2009.05.026

within ultrafast 2D MRI: one is an ability to deal with multiple chemical sites [15]; the other harnessed the spatial selectivity of this imaging method to develop a real-time compensation algorithm of the field inhomogeneities [16]. This latter algorithm used an a priori mapping of the global B_0 field to compensate for inhomogeneity effects during the acquisition itself, by way of manipulating the radiofrequency (RF) pulses and by suitably shaping the time-dependent acquisition gradients. More recently, an alternative scheme has been proposed for coping with T_2* effects which does not rely on a priori knowledge of the B_0 field distribution, but rather employs a self-refocusing sequence that directly produces a fully refocused image [17].

In this article, we further explore both of these inhomogeneity compensation algorithms, paying particular consideration to their generalization to large field of views (FOVs) and to limitations that arise with this transition. Special attention is paid to new self-refocused sequence variants, and to strategies that free the resulting images from most remaining spatial distortions via post processing. The next section starts with a brief overview of the spatial encoding approach as applied within a single-scan 2D imaging context, and continues with a qualitative comparison to its EPI counterpart.

2. Hybrid spatial-/time-encoded MRI: basic comparisons with EPI

A detailed description of the principles underlying spatially encoded MRI can be found in [16]. In its simplest, one-dimensional form, it is based on a spatially sequential excitation of the spin density profile $\rho(y)$, followed by an acquisition of the signal originating point-by-point from consecutive locations along the encoded y-axis. The ability to separately excite each position in the sample is achieved by a gradient that spreads the resonance frequency of the chemical site along a frequency axis, acting in unison with a frequency-swept (chirped) RF pulse, designed to progressively affect the sample over the targeted spatial axis [18–20]. Tuning spin nutation angles at each point according to the RF's coil efficiency and the sweeping rate R [12,19], enables one to impart a 90° excitation endowed with a quadratic phase profile given by:

$$\phi_{exc}(y) = -\frac{\gamma^2 G_{\mathrm{exc}}^2}{2R} y^2 + \frac{\gamma G_{\mathrm{exc}} O_f}{R} y - \frac{O_i^2}{2R} \tag{1}$$

Here G_{exc} is the excitation gradient, O_i and O_f are the initial and final offsets of the frequency chirp, and γ is the gyromagnetic ratio. The RF sweep rate will then be given by the time T_{exc} taken to excite the spins, according to $R = (O_f - O_i)/T_{\mathrm{exc}}$. The quadratic evolution phase in Eq. (1) allows one to reconstruct $\rho(y)$ by directly reading the spins' signal in the presence of an acquisition gradient G_a, owing to the fact that in the ensuing experiment the spins' phases will vary rapidly throughout the sample, except at a single stationary-phase point. According to the stationary-phase approximation, only spins within close vicinity of this point will have their magnetizations in-phase and contribute to a macroscopic observable, whereas spin-packets in all other regions will rapidly change their phases and interact destructively within their neighborhoods. The modulus of the acquired signal thus reflects the spin density's profile at a single pixel, whose size is determined by the "sharpness" of the stationary-phase region according to:

$$\Delta y_{SE} = \sqrt{\frac{2\pi}{\left|\partial^2 \phi_{\mathrm{exc}}/\partial y^2\right|_{y_{\mathrm{stationary}}}}} = \left|\frac{\sqrt{R}}{\gamma G_{\mathrm{exc}}}\right| \forall y \tag{2}$$

Contrary to traditional Fourier-based methods, where resolution depends on acquisition parameters such as the number of collected points $N = FOV_y/\Delta y$, it follows that in spatially encoded MRI, Δy_{SE} will be determined by the excitation parameters (in order to ensure this, the number of points digitized in these experiments will be generally made larger than $FOV_y/\Delta y_{\mathrm{SE}}$). The acquisition process will still

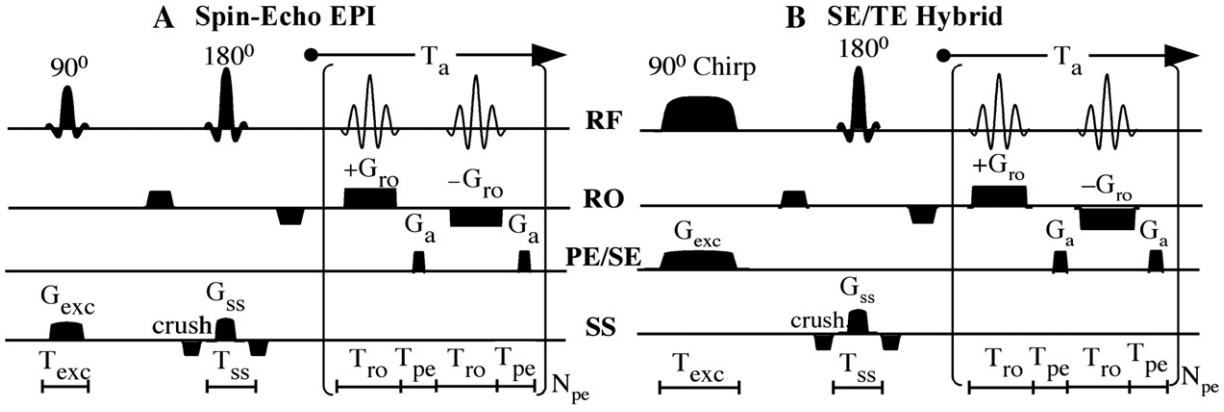

Fig. 1. Basic 2D single-scan pulse sequences and timing definitions (horizontal axis; delays not drawn to scale) used in 2D Spin-Echo EPI (A) and 2D spatial/time-encoded hybrid sequence (B). For both cases, the overall acquisition time is given by $T_a = 2(T_{ro} + T_{pe})N_{pe}$.

define the image's FOV: to unravel a targeted field FOV_y, G_a needs to be applied over an acquisition time T_a fulfilling $|G_{exc}T_{exc}|=|G_aT_a|$. When factoring in this demand, it follows that in order to match EPI's pixel resolution

$$\Delta y_{EPI} = [\gamma G_a T_a]^{-1}, \tag{3}$$

these methods need to increase their acquisition gradient by a factor of $\sqrt{N}$. A relatively straightforward way of avoiding this otherwise unacceptable penalty, arises upon considering the extension of this scheme to two dimensions, based on the incorporation of the spatial encoding along a phase-encoded (PE) axis, and use of a traditional time-domain encoding along the read-out (RO) dimension. The relatively soft gradient demands then placed along the PE axis make it easy to incorporate spatial encoding along this dimension. In this work we focus on this particular "hybrid" sequence and compare its performance vis-à-vis traditional 2D spin-echo EPI (Fig. 1). Notice that in these tests the RO channel acts similarly in both sequences, while the PE channel is replaced in the latter by a progressive spatial unraveling over $2N_{pe}$ steps. In both cases, the 3rd axis is used for slice selection.

Fig. 2. presents images acquired using these basic 2D spin-echo EPI and hybrid spatial-/time-encoded MRI schemes, on a 25-mm-diameter phantom. The top-row scans were collected under homogeneous $\Delta B_o \approx 0$ conditions, whereas the bottom set was collected under a moderately inhomogeneous $|\Delta B_o| \approx 200$ Hz environment. When the field is homogeneous, both sequences provide comparable single-scan images, each of them characterized by a minor artifact: a duplication of the imaged object at half FOV can be seen upon employing all the readout PE echoes for processing the EPI image (A); a progressive weighting is also evident along this axis in the spatially encoded acquisition, resulting from the sequential manner in which the spins were excited and then imaged along this domain (Fig. 2B). This problem can be resolved either by an additional post-processing renormalization step, or experimentally, by combining a pair of forward and reversed scans. Yet another alternative is discussed in the Section 3, based on a modified sequence designed to directly yield evenly T_2-weighted images.

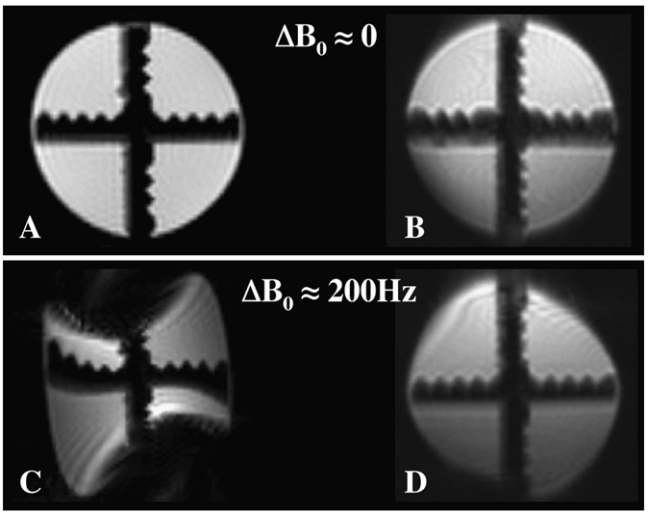

Fig. 2. 2D Images (FOV_x=FOV_y=25 mm) of a cross-shaped phantom filled with $CuSO_4$-doped water. Like all other images presented in this report, these data were acquired at 7 T on a 300/89 Varian VNMRS vertical-bore system (Varian Associated, Palo Alto, CA, USA) using a quadrature-coil probe having an overall volume of 30×30×46 mm^3. (A) 2D spin-echo EPI image (5-mm slice; T_{exc}=2.5 ms; T_{se}=3 ms; T_a=24 ms; Δx=Δy=0.4 mm); here the PE's FOV_y was increased by 100% in order to avoid ghosting artifacts. (B) Spatial/time-encoded hybrid image (4-mm slice; T_{exc}=4 ms; R_{chirp}=48 kHz/ms; T_a=40 ms; Δx=0.4 mm; Δy=1.1 mm). (C) 2D Spin-Echo EPI image arising upon subjecting the phantom to an inhomogeneous $|\Delta B_0| \approx 200$ Hz field (5-mm slice; T_{exc}=2.5 ms; T_{se}=2.5 ms; T_a=40 ms; Δx=Δy=0.5 mm). (D) Idem but upon collecting the image using a hybrid spatial/time-encoded sequence (5-mm slice; T_{exc}=5 ms; R_{chirp}=50 kHz/ms; T_{se}=2.5 ms; T_a=40 ms; Δx=0.5 mm; Δy=1.2 mm).

Fig. 2C and D illustrate the differing behaviors exhibited by these two sequences, when placing the same phantom in a moderately inhomogeneous B_0 environment. Although both images are affected by the ensuing ΔB_0, the EPI-derived image is far more distorted than its hybrid counterpart –particularly along the low-bandwidth (y-axis) direction. This difference between the sequences' abilities to deal with non-homogeneities can be rationalized by examining the mathematical expressions for the signals arising from each scheme. EPI's behavior in the presence of ΔB_0 inhomogeneities has been thoroughly described in literature [21,22], and involves adding a cumulative phase term that is proportional to the inhomogeneity's temporal evolution on top of the basic k-domain signal:

$$S^{EPI}(k_x,k_y) = \int\int \rho(x,y) e^{ik_x x + ik_y y + i\,\gamma \Delta B_0(x,y)\cdot[t - t_E]} dxdy \tag{4}$$

The k-space is defined here as $k_{x,y} \equiv \gamma \cdot \int G_{x,y}(t')dt'$, and t_E denotes the spin-echo refocusing time. Using standard manipulations [9,22,23] and assuming that the PE k_y axis is the one decoded monotonically with respect to t, one can rewrite this expression as:

$$S^{EPI}(k_x,k_y) = \int\int \rho(x,y) e^{ik_x x + ik_y y'} dxdy \tag{5}$$

This is similar to the homogeneous-case expression albeit with a distorted PE y' axis defined by

$$y' \equiv y + \frac{\Delta B(\vec{r}) \cdot [T_{ro} + T_{pe}]}{G_a \cdot T_{pe}} = y + \frac{\Delta B(\vec{r})}{\overline{G}_a}, \tag{6}$$

where for simplicity we define $\overline{G}_a$ as an averaged (rather than blipped) value of the effective PE acquisition gradient. Considering the similarity of the acquisition stages between the EPI and hybrid MRI sequences, the above expressions can be easily extended to derive the effects of ΔB_0 on the sequence shown in Fig. 1B. This requires adding the

quadratic phase term ϕ_{exc} imparted on the spins during their excitation:

$$S^{SE}(k_x,k_y)=\int\int\rho(x,y)e^{ik_xx}e^{-i\phi_{exc}(\hat{y})+ik_yy'}dxdy, \quad (7)$$

where

$$\phi_{exc}(\hat{y})=-\frac{\gamma^2G_{exc}^2}{2R}\hat{y}^2+\frac{\gamma G_{exc}O_f}{R}\hat{y}-\frac{O_i^2}{2R} \quad (8)$$

Notice that by contrast to Eq. (1), the $\hat{y}$ variable in ϕ_{exc} is in this case also distorted due to the effects of ΔB_0 during this excitation event. In the spatially encoded case, two separate distorted paths are thus to be considered: one relating to the excitation ($\hat{y}$) and the other to the acquisition (y') axes. Assuming for the sake of argument similar acquisition and excitation gradients, G_a=G_{exc}, these two paths will coincide, leading to an expression that is identical to the one in Eq. (6). This expression can be used to explain the different effects that a given field inhomogeneity will have on the two ultrafast MRI experiments. For both sequences, the model predicts that ΔB_0 will affect the low bandwidth axis in a fashion that is inversely proportional to the acquisition gradient strength. However, while in the EPI case this gradient is set by the minimal required FOV via $FOV_{PE}=2\pi/\gamma G_aT_{pe}$, in the hybrid MRI sequence, the spatial resolution is given by Eq. (2) and the gradient's strength will be limited mostly by the hardware specifications and by artifacts such as diffusion or eddy currents. It follows that the stronger acquisition gradients that need to be used in this latter case for achieving an EPI-like resolution, help to maintain ΔB_0 artifacts at reasonably small levels while still enjoying a full utilization of the system's hardware.

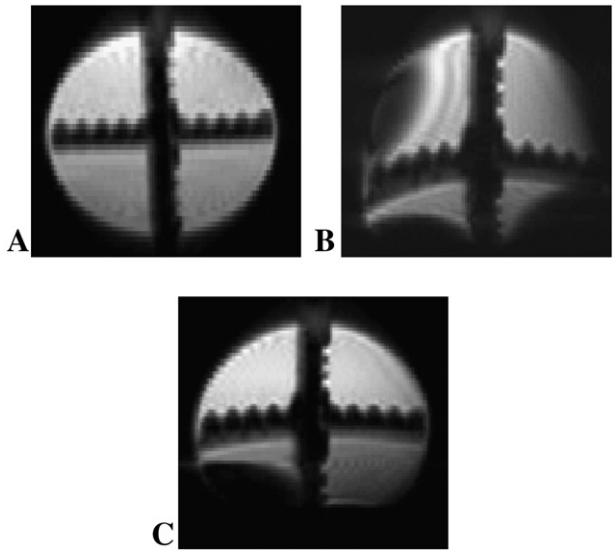

Fig. 3. 2D Spin-echo hybrid imaging (Fig. 1B) of a cross shaped phantom (FOV_x=FOV_y=25 mm) filled with $CuSO_4$-doped water (5-mm slice; T_{exc}=5 ms; R_{chirp}=34 kHz/ms; T_{se}=2.5 ms; T_a=40 ms; Δx=0.4 mm; Δy=1.0 mm). (a) Homogeneous B_0 field [$\Delta B_0 \leq 150$ Hz] image. (b) ΔB_0 inhomogeneity of ca. 2.2 kHz along the y-axis. (c) Image, taken under similar conditions as in (b), but using pulses and gradients, both designed using the real-time inhomogeneity compensation algorithm. Pulse shapes were calculated using the Shinnar-LeRoux algorithm [24]. Echo time ranges between 5 and 50 ms, depending on the slice location along the vertical axis of the sample.

3. Inhomogeneity corrections using a real-time compensation algorithm

Spatially encoded MRI addresses and detects spins at specific parts of the sample over time. It was recently proposed that this feature could be exploited to develop an inhomogeneity compensation algorithm, based on the active correction of ΔB_0 effects during the course of excitation and acquisition events [16]. This section briefly recapitulates the key steps of this compensation, and explores its relevance for a variety of 2D MRI scenarios. The basic conditions that need to be restored when acquiring a spatially encoded image under the influence of field inhomogeneities are: (i) keeping a constant pixel size, and (ii) retaining a linear relation between time and space throughout the acquisition. Starting from Eq. (2), these conditions can be mathematically expressed by:

$$\frac{\partial}{\partial t}\left(\frac{\partial^2\left[\phi_{exc}(y)+\gamma G_a(t)yt+\gamma\Delta B_0(\vec{r})t\right]}{\partial y^2}\Big|_{y_{stationary}}\right)=0\ \forall y \quad (9)$$

$$y_{stationary}(t)=-\frac{FOV_y}{2}+\frac{FOV_y}{T_a}t \quad (10)$$

where T_a is the total acquisition duration (caption, Fig. 1) and $y_{stationary}(t)$ denotes the acquisition route along the spatially encoded axis. The second-derivative in Eq. (9) depends on the excitation phase, as well as on an inhomogeneity-driven evolution during the acquisition stage. Accordingly, the constant pixel size condition can be reached by superimposing on the ideal chirped excitation a phase correction profile that is based on an a priori knowledge of ΔB_0. The second (linearity) condition relates in turn solely to the acquisition stage: field inhomogeneities will cause in this case a nonlinear transition of the stationary-phase-point from one end of the sample to the other. Imposing on G_a a time-dependency that matches these field distortions can compensate for this effect, in such a way that the linear relation in Eq. (10) is restored. It is worth reiterating that both the RF and gradients' manipulations employed by this algorithm are feasible, owing to the one-to-one time/space relations which form the basis of spatially encoded MRI.

Upon proceeding towards the integration of this one-dimensional (1D), real-time inhomogeneity compensation algorithm into a 2D hybrid encoding sequence of the kind depicted in Fig. 1B, one should notice that, by contrary to the 1D case discussed in [16], this 2D sequence treats the PE readout in a noncontinuous fashion. This forces the segmentation of the time-dependent $G_a(t)$ into a series of

piecewise constant gradients; taking T_{pe} to denote the duration of such "blipped" gradients, each event in the series will now contain an average value given by

$$\overline{G_a^{(i)}} = \frac{1}{T_{pe}} \int_{t_{i-1}}^{t_i} G_a(t')dt' \tag{11}$$

Since the cumulative effect of the continuous and blipped gradients is similar, deviations from an ideal correction will be confined within the scope of a single readout/phase-encode cycle. Fig. 3 illustrates the efficiency of this inhomogeneity compensation algorithm for a 2D image, involving a 1D ΔB_0 inhomogeneity of about 2.2 kHz extending along the vertical (spatially encoded) axis. The correction makes a good reinstatement of the ideal image shape. Still, main variations in the signal strength are visible as a result of horizontal readout slices having different echo-times, as well as of certain regions falling outside this algorithm's compensating abilities.

While this example relates to 2D imaging, the inhomogeneity compensation algorithm as embodied by Eqs. (9,10) deals solely with one-dimensional ΔB_0 inhomogeneities. A successful application of this imaging algorithm therefore depends on finding a 1D orientation that governs the inhomogeneity pattern. A main limiting aspect of this compensation approach therefore emanates, particularly for larger FOV systems, from the inhomogeneities along the axis that is perpendicular to the corrected, PE orientation. Indeed given a 2D inhomogeneity $\Delta B_0(x,y)$ of an object, the input to the compensation algorithm will be a projection of such 2D map along a specific 1D orientation. For instance, this algorithm's corrections along the y-axis of an $N_x \times N_y$ plane would focus on 1D inhomogeneity projections given by:

$$\overline{\Delta B_0(y_n)} = \frac{\sum_{i=1}^{N_x} \Delta B_0(x_i, y_n)}{N_x} \qquad n \in [1..N_y] \tag{12}$$

Clearly, if the inhomogeneity variation along the perpendicular x-axis exceeds a certain limit, this 1D projection will no longer represent correctly the ΔB_0 2D pattern to be compensated: neither the encoding phases nor the acquisition gradients calculated by the algorithm will then be accurately tuned to the local field variations, leading to sizable distortions for different x-coordinates. As exemplified in Fig. 4 for synthetic data sets that exclude/include a standard deviation (S.D.) in the values spread by the $\overline{\Delta B_0(y_n)}$ distributions, this can significantly degrade the quality of the fix.

4. Self-refocused, spatially encoded MRI sequences

The preceding section delineated strengths and weaknesses arising in spatially encoded MRI, upon attempting to tailor RF pulses and gradients so as to specifically match the effects of 1D inhomogeneity patterns. Stimulated by the limitations highlighted in Fig. 4, this section introduces an alternative that employs a different approach to remove ΔB_0

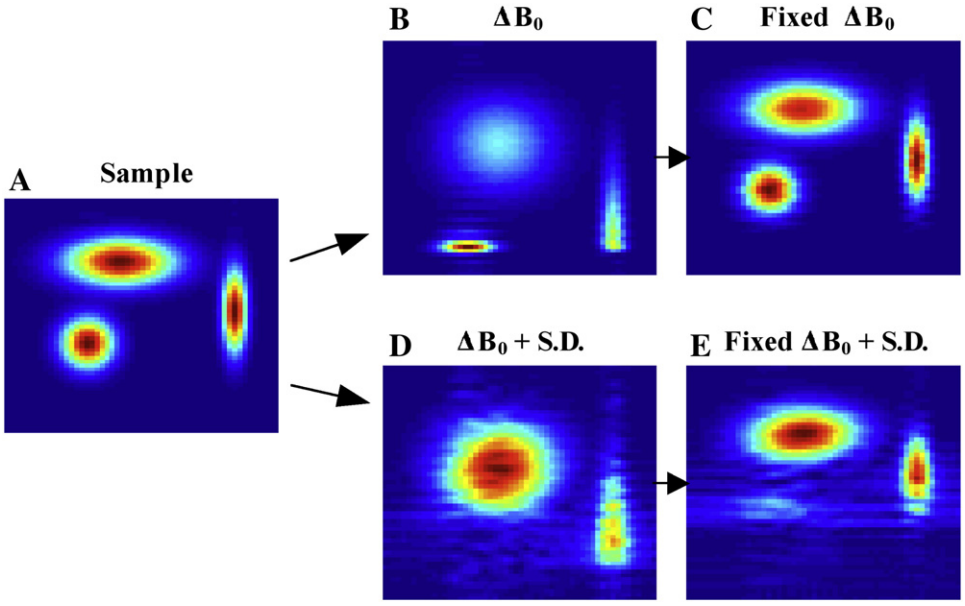

Fig. 4. Simulations of adding a standard deviation (S.D.) (y) effect on the inhomogeneity fix algorithm along the y-axis (ordinate). (A) Hybrid NMR image assumed in a homogeneous B_0 field. (B) Image acquired upon subjecting the sample to a ΔB_0 inhomogeneity of 1.2 kHz, solely along the y-axis. (C) Idem as in (B), upon applying the real-time compensation algorithm. (D) Image acquired upon subjecting the sample to a ΔB_0(y) of 1.2 kHz but this time with a S.D. of 10% along the orthogonal x-axis. (E) Idem as in (D), after applying the real-time compensation algorithm. The ΔB_0 variation along the x-axis is seen to degrade the quality of the correction. For all cases Δx=0.05 mm; Δy=0.6 mm; FOVx=2 mm; FOVy=10 mm.

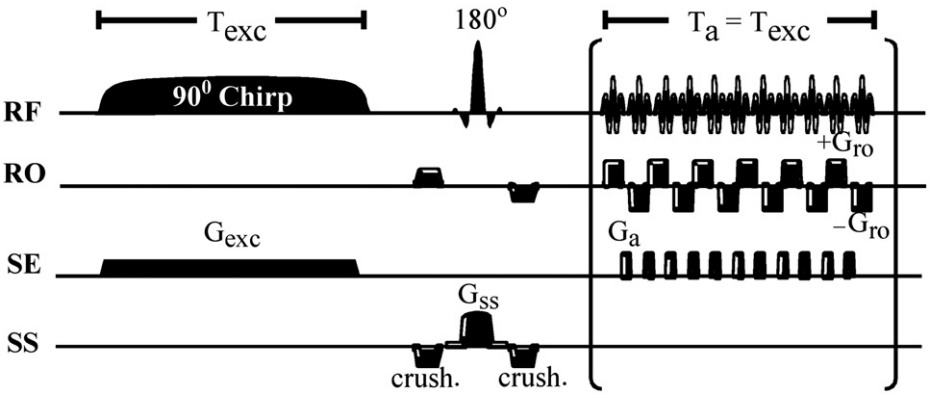

Fig. 5. Self-refocused, T_2*-compensated version of a 2D hybrid single-scan MRI sequence.

artifacts from 2D hybrid images based on the generation of a spin-echoing of all the internally derived shifts, for each and every readout event throughout the decoding sequence. Fig. 5 portrays the idea behind such sequence, which is based on adjusting the scheme in Fig. 1B so as to equal the excitation and acquisition durations, and then symmetrically separating these with a 180° spin-echo pulse. Each line's readout event along the spatially encoded axis will thereby coincide with its own specific spin-echo time, effectively refocusing all ΔB_0 and chemical shift distortions for each and every particular PE voxel. This in turn opens the possibility of refocusing T_2* effects in a model-free fashion.

Fig. 6 compares 2D images arising from spin-echo EPI and from this new self-refocused, T_2*–compensated hybrid MRI sequence, on a phantom containing an intrinsic local inhomogeneity resulting from water-Teflon and water-glass interfaces. Although the inhomogeneity span within the sample is rather moderate (~250 Hz), it clearly poses a challenge for EPI, whereas a simple and successful reconstruction of the image is achieved using the self-refocused sequence in Fig. 5.

Like all other spatially encoded images presented so far, the PE profile in Fig. 6B shows a decay along the y-axis stemming from the increased T_2 weighting of the pixels along this spatially encoded direction. Going one step further, it is possible to extend the self-refocusing T_2*-compensation in the sequence of Fig. 5, to produce images with a constant T_2-weighting along this vertical direction. This can be achieved by replacing the broadband spin-echo pulse with a frequency-swept chirped 180° pulse that imparts a similar refocusing, yet inverts the pixels along the y-axis in a sequential manner (Fig. 7). In addition to appearing fully refocused, all lines that were spatially encoded will thus experience the same transverse evolutions by the times their signals are detected. This in turn produces a spatially-uniform T_2 weighting, allowing the sequence to be regarded as a legitimate way of achieving T_2-based contrast in an ultrafast 2D MRI context.

Further insight on this scheme can be gained by examining the phase manipulations undergone by the spins during the three equally timed excitation/refocusing/acquisition stages, which follow the initial slice-selection block in Fig. 7. The chirped 90° pulse will re-excite the spins within a selected slice, and impart on them a quadratic phase profile $\phi^{(1)}_{\mathrm{exc}}(y)$ as expressed in Eq. (1). Apart from reversing the spins' phases, the subsequent spin-echo 180° chirp adds a quadratic phase profile of its own [16]:

$$\phi_{180}(y) = -\frac{(\gamma G_{\mathrm{exc}})^2}{R} y^2 \tag{13}$$

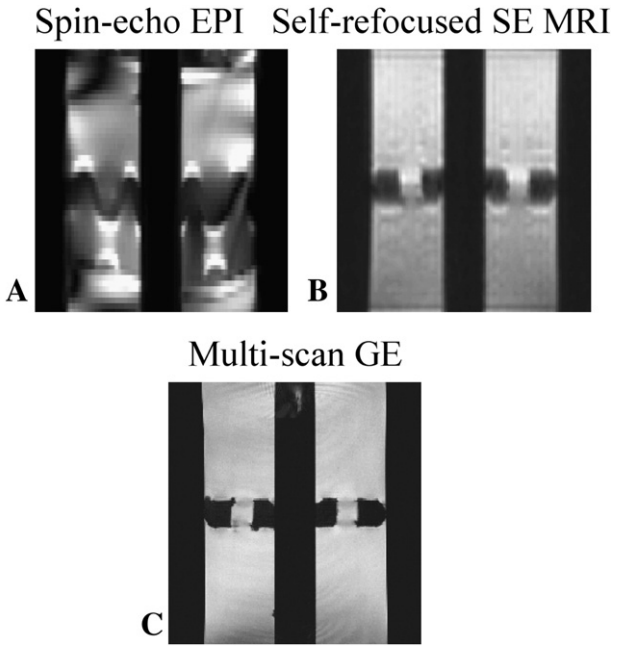

Fig. 6. EPI vs. self-refocused hybrid images of a phantom containing a 5 mm glass tube (FOV_y=32 mm, vertical) and a 5 mm Teflon disc (FOV_x=30 mm, horizontal) embedded in a 25 mm $CuSO_4$-doped water tube. Similar parameters were used for acquiring both images. (A) Spin-echo EPI [0.5-mm slice; T_{exc}=5 ms; T_{se}=3 ms; T_a=40 ms; Δx=0.3 mm; Δy=0.6 mm]. (B) Spin-echo hybrid sequence in Fig. 5 (0.7-mm slice; T_{exc}=24 ms; R_{chirp}=1 kHz/ms; T_{SE}=3 ms; T_a=24 ms; Δx=0.5 mm; Δy=1.2 mm]. (C) Reference multi-scan gradient-echo image acquired under ideal conditions. The B_0 field was shimmed to the best possible setting, producing field variations of ca. 250 Hz over the presented FOV.

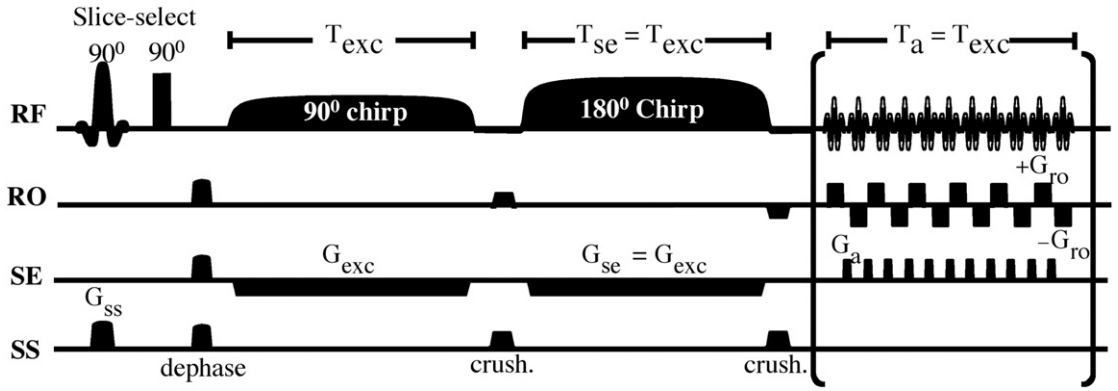

Fig. 7. 2D Hybrid ultrafast MRI sequence with even-T_2 weighting and full T_2∗ refocusing.

Subtracting $\phi_{\text{exc}}^{(1)}(y)$ from this expression thus yields the preacquisition phase profile:

$$\phi_{\text{exc}}^{(2)}(y) = -\frac{\gamma^2 G_{\text{exc}}^2}{2R}y^2 - \frac{\gamma G_{\text{exc}} O_f}{R}y - \frac{O_i^2}{2R} \tag{14}$$

Comparing the resulting phase profile with the one given in Eq. (1), we notice that the only difference between the two lies in the sign of the linear term. This change actually signifies a shift of the stationary phase location, from one end of the spatially encoded axis (e.g., $-FOV_y/2$), to the opposite ($+FOV_y/2$). Constant-time T_2-weighting is thus achieved by exciting and acquiring in the same direction along this axis, resulting in equal transverse evolutions for all spatial lines.

Fig. 8 illustrates how this sequence replaces the progressive T_2 weighting otherwise characterizing hybrid images, with a spatially homogeneous T_2 contrast. Chosen for this test was a phantom made up by an inner $CuSO_4$-doped water tube, placed within a distilled H_2O vessel characterized by a transverse relaxation time that is ca. eight times as long. When compared against their EPI counterpart image (Fig. 8A), it is clear that both spatially encoded sequences presented in Figs. 5 and 7 successfully remove most residual ΔB_o-derived distortions. When comparing among the results afforded by these last two sequences (Fig. 8B and C), it is also clear that the latter also eliminates the progressive relaxation spatial bias, and leads to a genuine T_2-only-based contrast.

In addition to an even T_2 weighting, the full T_2*-refocusing provided by the frequency-swept 180° pulse in Fig. 7 can be valuable when considering challenging imaging scenarios, like the one posed by single-scan animal MRI in vertical-bore systems. Fig. 9 shows this for a murine brain axial slice, imaged using this extended self-refocusing constant-time sequence. Poor shimming conditions provided an inhomogeneity range of 600–800 Hz, and prevented the acquisition of meaningful EPI images. Still, apart from sensitivity losses, the constant-T_2 and T_2*-compensated spatially encoded approach succeeds in providing all basic structural features.

Notwithstanding the last two examples, where reasonable "as-collected" images resulted from hybrid sequences in the presence of moderate field inhomogeneities, higher ΔB_0 values will result in distinct distortions — chiefly along the weaker-gradient PE axis. These artifacts can, however, be compensated to a high degree using postprocessing procedures. Several such approaches were developed over the years to alleviate inhomogeneity artifacts in EPI [9,22,25,26]; similar formalisms can be developed to deal with ΔB_0 effects in spatially encoded sequence variants. Based on an a priori knowledge of the ΔB_0 map, we

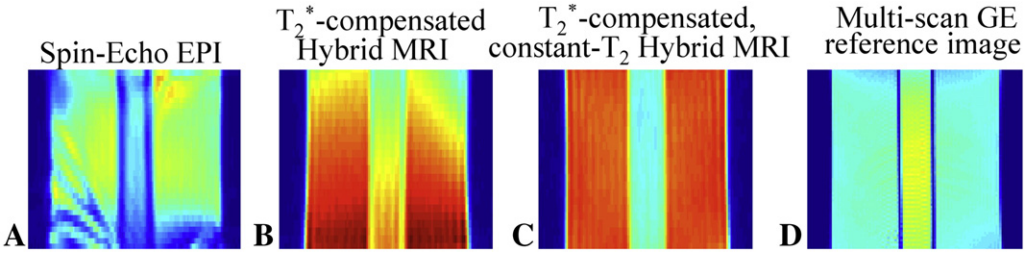

Fig. 8. NMR images of a phantom (FOV_x=27 mm; FOV_y=24 mm) made up of an inner 5 mm glass tube containing $CuSO_4$-doped water (T_2=50 ms), placed inside a 25 mm diameter distilled water tube (T_2=400 ms). (A) Spin-echo EPI (1-mm slice; T_{exc}=2 ms; T_{se}=30 μs; T_a=24 ms). (B) T_2∗-compensated Spin-echo hybrid image; given the parameters chosen (sequence in Fig. 5 with a 2-mm slice; T_{exc}=9 ms; R_{chirp}=9.5 kHz/ms; T_{SE}=4 ms; T_a=9 ms; Δx=0.4 mm; Δy=1.2 mm), the differential T_2 spatial weighting in the two tubes are accentuated. (C) Spin-echo hybrid image involving T_2*-compensation and even T_2 weighting (sequence in Fig. 7 with 2-mm slice; T_{exc}=9 ms; R_{chirp}=9.5 kHz/ms; T_{SE}=9 ms; $R_{chirp\text{-}180}$=9.5 kHz/ms; T_a=9 ms; Δx=0.4 mm; Δy=1.2 mm), leading to a spatially unbiased T_2 contrast between the two sample compartments. (D) Reference multiscan gradient-echo image acquired under ideal conditions. In all cases, the B_0 field was shimmed to the best possible setting, producing field variations of ca. 500 Hz over the presented FOVs.

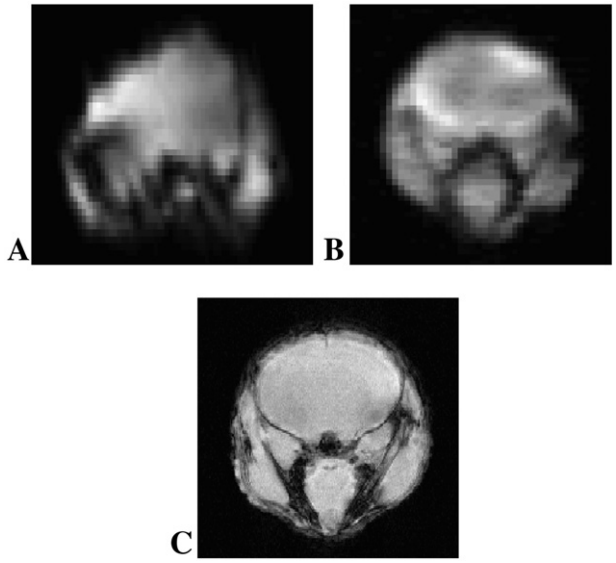

Fig. 9. Cross-sectional images (FOV_x=FOV_y=17 mm) of a murine brain. (A) Spin-echo EPI (1-mm slice; T_{exc}=2 ms; T_{se}=4 ms; T_a=24 ms; Δx=0.3 mm; Δy=0.8 mm). (B) Constant-T_2 and T_2*-refocused 2D hybrid MRI (sequence in Fig. 7 with 0.2-mm slice; T_{exc}=24 ms; R_{chirp}=0.9 kHz/ms; T_{SE}=24 ms; T_a=24 ms; Δx=0.3 mm; Δy=1.0 mm). (C) Reference multi-scan gradient-echo image.

developed one such protocol that re-registers each pixel back to its original location, while restoring its undistorted intensity. This approach starts by rewriting Eq. (7) for a signal acquired in a non-homogeneous environment, this time under the assumption of equal excitation and acquisition paths condition:

$$S^{SE}(k_x,k_y)=\int\int\rho(x,y)e^{ik_x x}e^{-i\phi_{exc}(\hat{y})+ik_y\hat{y}}dxdy \tag{15}$$

The ΔB_0 effects are here summarized in a distorted $\hat{y}$ axis modeled as in Eq. (6), while distortions along the perpendicular x-axis are neglected given the characteristic short readout durations (100–300 μs) and the typically strong gradients applied along this direction. Processing the signal in Eq. (15) into an undistorted image involves then two stages: the first relates to the time encoded x-axis and involves a conventional 1D Fourier transform; the second relates to the spatially encoded y-axis and involves the stationary-phase-approximation. The former procedure is straightforward; the latter approximation requires transforming first the integral in Eq. (15) into a modified $(x,\hat{y})$ coordinate system as

$$S^{SE}(k_x,k_y)=\int\int\tilde{\rho}(x,\hat{y})e^{ik_x x}e^{-i\phi_{exc}(\hat{y})+ik_y\hat{y}}dxd\hat{y} \tag{16}$$

$$\tilde{\rho}(x,\hat{y})=\rho(x,\hat{y})J(\hat{y}) \tag{17}$$

$$J(\hat{y})=\frac{\partial y(x,\hat{y})}{\partial\hat{y}}=1-\frac{1}{\overline{G}_a}\frac{\partial\Delta B(x,\hat{y})}{\partial\hat{y}} \tag{18}$$

where $J(\hat{y})$ is a Jacobian defined by the derivative of the original vs. the distorted y-axes. This term describes the spatial deformation of a pixel when transformed from a (x,y) to a $(x,\hat{y})$ coordinate system, and reduces to unity in the absence of field inhomogeneities. Fourier transformation and application of the stationary phase approximation

$$S^{SE}(k_x,k_y)\xrightarrow[SPA_y]{FT_x}\tilde{\rho}(x,\hat{y}) \tag{19}$$

provides the sought 2D image profile, albeit in the ΔB_0–distorted coordinate system. Reverting to the original coordinates can be done via a $\hat{y}\rightarrow y$ transformation followed by a pixel intensity restoration, based on reversing the relation in Eq. (17). A possible complication that may emerge in this step involves an attenuation or peaking of a pixel's intensity, resulting from Jacobian values that diverge or are close to zero, respectively. Such anomalies may arise from areas for which the ΔB_0 map is not well defined; these pixels should be excluded, thereby limiting the maximal ΔB_0 distortions that can be successfully reconstructed.

Fig. 10 illustrates the potential of this reconstruction procedure, when executed within the context of the self-refocusing variant introduced in Fig. 7. These images were characterized by a ΔB_0 inhomogeneity of ~4.5 kHz; spin-echo EPI images acquired under these conditions (not shown) exhibited no resemblance to the actual sample. The basic hybrid sequence of Fig. 1B leads to a discernable yet poor reconstruction over most of the scanned FOV (Fig. 10A). Applying any of the self-refocusing sequence variants, however, led to significantly better results, effectively unwrapping most of the spin dephasing and rendering an image that is almost fully in phase (Fig. 10B).

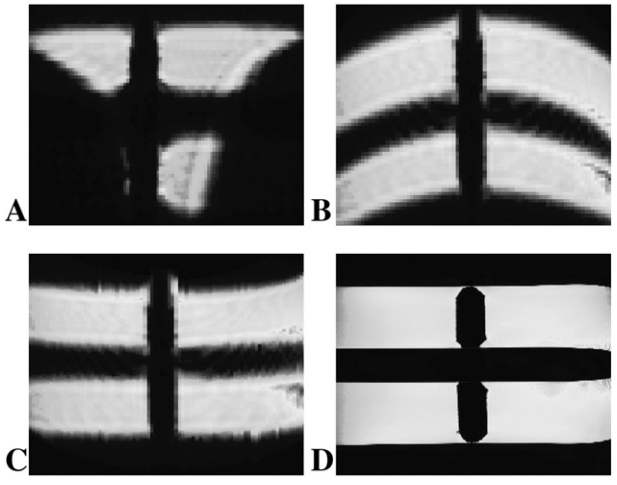

Fig. 10. Hybrid 2D images of the phantom used in Fig. 6 laid horizontally (FOV_x=40 mm; FOV_y=30 mm) and subjected to a field inhomogeneity of ~4.5 kHz. (A) Image arising from the basic hybrid sequence in Fig. 1B (1-mm slice; T_{exc}=4 ms; R_{chirp}=22 kHz/ms; T_{se}=3 ms; T_a=24 ms; Δx=0.5 mm; Δy=1.6 mm]. (B) Idem as in (a) but for the self-compensated sequence in Fig. 7 (1-mm slice; T_{exc}=24 ms; R_{chirp}=0.5 kHz/ms; T_{SE}=24 ms; T_a=24 ms; Δx=0.5 mm; Δy=1.7 mm). (C) Idem as in (B) after subjecting pixels to a post-processing re-registration based on the corresponding ΔB_0 field map. (D) Reference multi-scan gradient-echo image.

Nevertheless, the resulting y-profile remains reconstructed in a distorted coordinate system. Subsequent application of the pixel registration algorithm of Eqs. (16–19) produced the nearly undistorted image in Fig. 10C, which exemplifies the potential of this integrated acquisition/postprocessing scheme.

5. Conclusions and perspectives

Spatial encoding was originally developed for collecting multidimensional NMR spectra within a single scan. The same principles can also be exploited to collect single-scan 2D NMR images, an aim for which MRI already possesses well-established, EPI-derived techniques. The EPI family of sequences has a proven ability to produce 2D images and makes the most efficient use of the gradients' capabilities per unit time; still, spatial encoding techniques could prove advantageous when operating in the presence of internal resonance frequency shifts. In this report, we concentrated on exploring this as a mean to deal with non-homogeneous environments and established the potential of this approach as an efficient imaging method, based on a hybrid sequence variant where the phase-encoded low-bandwidth channel was replaced with a spatial encoding. This approach's robustness vis-à-vis main field inhomogeneities and internal susceptibility variations was thus examined in four successive stages of improvement. First, the intrinsic increases in gradient strength required by spatially encoded MRI for its operation showed an ensuing immunity to ΔB_0 distortions. Robustness could be further extended by a real-time approach designing RF encoding and gradient-driven decoding waveforms, on the basis of the field ΔB_0(x,y) map. Further generality was provided by self-refocusing sequences capable of sequentially spin-echoing the T_2* dephasing throughout the course of the acquisition, via a special timing of the encoding and decoding processes. Finally, an additional benefit was shown upon introducing, on top of the self-refocusing sequence, a constant time encoding-decoding variation, which permits a genuine T_2 weighting of the single-scan 2D MR images. An appealing aspect of these latter self-refocusing techniques is that, by contrast to previously described alternatives, they no longer need mapping of the field inhomogeneities in order to correct for them. Still, if a field map acquisition is an option [22,27,28], post-processing of the self-refocused signal can yield undistorted images even under conditions which render the use of EPI impractical.

Notwithstanding all these promising results, issues remain to be resolved before hybrid techniques like the ones here presented, can be exploited in common in vivo applications. Specific absorption rate (SAR) restrictions for instance ought to be evaluated, taking into consideration the relatively high bandwidths that characterize chirped pulses; an initial formalism evaluating these effects is presented in the Appendix A. Another issue requiring further investigation concerns the method's effective spatial resolution when compared to time-encoding methods. As mentioned, theoretical derivations based on the stationary phase approximation yield, for identical gradient strengths, a spatially encoded pixel size that exceeds by a factor of $\sqrt{N}$ its EPI counterpart. This comparison, however, should not be taken as an ultimate limit since (i) gradient strengths are not always the limiting factor, and (ii) additional processing approaches suggest that spatially encoded signals could be manipulated to produce a higher resolution than currently achieved, by subjecting them to more complex manipulations than just a magnitude calculation.

Transitioning from the basic sequence to the self-refocused 2D hybrid variants offers a much higher immunity to field inhomogeneities — yet not without penalties. The main drawback relates to the longer T_{exc}'s characterizing the latter techniques; a possible solution to this problem involving multistationary-points encoding processes, is currently being investigated. Another aspect in need of improvement is the slice selection method used by the self-refocusing sequences (e.g., Fig. 7); currently, this is based on a basic excite/store combination, suboptimal within the context of multislice applications since during the acquisition all sample regions outside the specific slice being measured will be out of equilibrium. A possible solution for dealing with this issue is to integrate the slice selectivity and the frequency swept excitation into a single two-dimensional slice-selective chirped pulse, capable of simultaneously executing both tasks. We trust to report on these and other aspects of single-scan spatially encoded MRI in upcoming reports.

Acknowledgments

This research work was supported by the Israel Science Foundation (ISF 1206/05) and by the generosity of the Perlman Family Foundation. Y.S. acknowledges the Clore Foundation for a Graduate Fellowship.

Appendix A. SAR consideration in spatially encoded MRI

An important practical aspect in MRI relates to SAR limitations. Due to the gradient involved in the chirped excitation, the accompanying frequency swept RF pulses require higher bandwidth than the normal slice selective pulses used in traditional time-encoding imaging. We therefore deem it necessary to explore the relations between the spatial encoding parameters and the resulting SAR expected in this experiment. As known, a pulse's SAR is proportional to its power-squared, integrated over time [29]:

$$SAR \propto \int (B_1)^2 dt \tag{A.1}$$

For chirped pulses the power directly relates to the sweeping rate parameter R via [12]

$$B_1 \propto \sqrt{R}; \tag{A.2}$$

given a pulse duration T_{exc}, the rate will be:

$$R \propto \gamma G_{exc} L / T_{exc} \tag{A.3}$$

where G_{exc} denotes the accompanying excitation gradient. Setting Eqs. (A.2) and (A.3) into (A.1), the SAR dependency can be reduced to the product of the excitation gradient and the length of the spatially encoded axis yielding:

$$SAR \propto G_{exc} L \tag{A.4}$$

A similar derivation can be worked out for conventional slice-selective pulse, where the amplitude of B_1 depends on the bandwidth $\gamma G_{exc} T_{exc}$ and is inversely proportional to the pulse duration T_{exc}. Using the general SAR expression in (A.1) once more, we get the same dependency as in (A.4). The dissimilarity between the time and spatial encoding schemes emerges then from the different role of the excitation gradient in both cases. For time-encoded imaging, this gradient is used for slice selection and can be designed so as to avoid high amplitude values. Hybrid schemes, on the other hand, use this gradient in order to span the sample's resonance frequencies along a spectral axis, while its strength determines the image resolution via the relation in Eq. (2). Combining the latter with Eq. (A.4) reveals an underlying tradeoff between the image resolution and the SAR:

$$\mathrm{SAR} \propto \frac{1}{\Delta y_{SE}^{\,2}} \tag{A.5}$$

Given this proportionality relation as a quantitative safety indicator, the resulting practical implications are currently being explored upon by performing spatially encoded MRI on a whole body imaging system which monitors and enforces the SAR limitations.

References

[1] Stehling MK, Turner R, Mansfield P. Echo-planar imaging: magnetic resonance imaging in a fraction of a second. Science 1991;254:43–50.

[2] Bernstein MA, King KF, Zhou XJ. Handbook of MRI pulse sequences. Elsevier Academic Press; 2004.

[3] Speck O, Stadler J, Zaitsev M. High resolution single-shot EPI at 7T. Magma (New York, N Y) 2007;21:73–86.

[4] Beutel J, Kundel LH, Van Metter LR. Magnetic resonance imaging. Handbook of Medical Imaging. New York: SPIE Press; 2000.

[5] Ogawa S, Lee TM, Kay AR, Tank DW. Brain magnetic resonance imaging with contrast dependent on blood oxygenation. Proc Natl Acad Sci 1990;87:9868–72.

[6] Xiaoping H, Tuong HL. Artifact reduction in EPI with phase-encoded reference scan. Magn Reson Med 1996;36:166–71.

[7] Kadah YM, Hu X. Simulated phase evolution rewinding (SPHERE): a technique for reducing B0 inhomogeneity effects in MR images. Magn Reson Med 1997;38:615–27.

[8] Wan X, Gullberg GT, Parker DL, Zeng GL. Reduction of geometric and intensity distortions in echo-planar imaging using a multireference scan. Magn Reson Med 1997;37:932–44.

[9] Chang H, Fitzpatrick MJ. A technique for accurate magnetic resonance imaging in the presence of field inhomogeneities. IEEE Trans Med Imaging 1995;11(3):319–29.

[10] Hennig J, Mueri M. Fast imaging using burst excitation pulses. Abstracts of the society of Magn Reson Med; 1988. p. 238.

[11] Lowe IJ, Wysong RE. DANTE ultrafast imaging sequence (DUFIS). J Magn Reson B 1993;101:106–9.

[12] Shrot Y, Frydman L. Spatially encoded NMR and the acquisition of 2D magnetic resonance images within a single scan. J Magn Reson 2005; 172:179–90.

[13] Frydman L, Scherf T, Lupulescu A. The acquisition of multi-dimensional NMR spectra within a single scan. Proc Natl Acad Sci U S A (Online) 2002;99(25):15858–62.

[14] Shrot Y, Frydman L. Single-scan NMR spectroscopy at arbitrary dimensions. J Am Chem Soc 2003;125:11385–96.

[15] Tal A, Frydman L. Spectroscopic imaging from spatially-encoded single-scan multidimensional MRI data. J Magn Reson 2007;189: 46–58.

[16] Tal A, Frydman L. Spatial encoding and the acquisition of high definition MR images in inhomogeneous magnetic fields. J Magn Reson 2006;181:179–94.

[17] Chamberlain R, Park YJ, Corum C, Yacoub E, Ugurbil K, Jack Jr CR, Garwood M. RASER: a new ultrafast magnetic resonance imaging method. Magn Reson Med 2007;58:794–9.

[18] Kunz D. Use of frequency-modulated radiofrequency pulses in MR imaging experiments. Magn Reson Med 1986;3:377–84.

[19] Pipe JG. Spatial encoding and reconstruction in MRI with quadratic phase profiles. Magn Reson Med 1995;33:24–33.

[20] Pipe JG. Analysis of localized quadratic encoding and reconstruction. Magn Reson Med 1996;36:137–46.

[21] Schmitt F, Stehling MK, Turner R. Echo-planar imaging — theory, technique and applications. Berlin: Springer-Verlag; 1998.

[22] Jezzard P, Balaban RS. Correcting for geometric distortions in echo planar images from B0 variations. Magn Reson Med 1995;34:65–73.

[23] Farzaneh F, Riederer SJ, Pelc NJ. Analysis of T2 limitations and off-resonance effects on spatial resolution and artifacts in echo-planar imaging. Magn Reson Med 1990;14:123–39.

[24] Pauly JM, LeRoux P, Nishimura DG, Macovski A. Parameter relations for the Shinnar–LeRoux selective excitation pulse design algorithm. IEEE Trans Med Imaging 1991;10:53–65.

[25] Irarrazabal P, Meyer CH, Nishimura DG, Macovski A. Inhomogeneity correction using an estimated linear field map. Magn Reson Med 1996; 35:278–82.

[26] Sekihara K, Kohno H. Image restoration from nonuniform static field influence in modified echo-planar imaging. Med Phys 1987;14(6): 1087–9.

[27] Van Zijl PCM, Sukumar S, Johnson MO, Webb P, Hurd RE. Optimized shimming for high-resolution NMR using three-dimensional image-based field mapping. J Magn Reson, Series A 1994;111:203–7.

[28] Windischberger C, Robinson S, Rauscher A, Barth M, Moser E. Robust field map generation using a triple-echo acquisition. J Magn Reson Imaging 2004;20:730–4.

[29] Nguyen UD, Brown SJ, Chang IA, Krycia J, Mirotznik MS. Numerical evaluation of heating of the human head due to magnetic resonance imaging. IEEE Trans Biomed Eng 2004;51(8):1301–9.